ACS APPLIED MATERIALS & INTERFACES

www.acsami.org

Research Article

Interfacial Anchoring of CeO_2 on $Cu(OH)_2$ Nanoneedle Arrays for Corrosion-Resistant and Patternable Superhydrophobic Copper Surfaces

Runxiang Tan, Kaiwen Yang, and Jian Mao*

Cite This: *ACS Appl. Mater. Interfaces* 2026, 18, 48405−48416

Read Online

ACCESS | Metrics & More | Article Recommendations | Supporting Information

ABSTRACT: Conventional superhydrophobic copper surfaces typically rely on organic or fluorinated low-surface-energy modifiers, complicating fabrication and raising environmental concerns. Here, patternable superhydrophobic copper surfaces were fabricated by electrodepositing CeO_2 onto in situ-grown $Cu(OH)_2$ nanoneedle arrays. The arrays provided preconstructed rough scaffolds and favorable interfaces for CeO_2 loading. CeO_2 deposition preserved the integrity of the nanoneedle framework while introducing additional surface roughness. Subsequent vacuum heating promoted surface dehydration and dehydroxylation, thereby reducing the affinity of the surface for water. These changes, together with hierarchical roughness and the relative enrichment of nonpolar carbonaceous species, promoted the formation of a low-adhesion superhydrophobic state. The resulting surface exhibited a water contact angle of 157.6° and a water droplet adhesion force of 21.4 μN, together with mechanical durability, self-cleaning ability, and a corrosion inhibition efficiency of 99.162% in chloride-containing media. Selective heat treatment enabled the fabrication of patterned superhydrophilic/superhydrophobic regions, and the method was extended to copper mesh and copper foam. This work provides a strategy for constructing structurally controlled, multifunctional superhydrophobic protective surfaces without intentionally added organic or fluorinated modifiers.

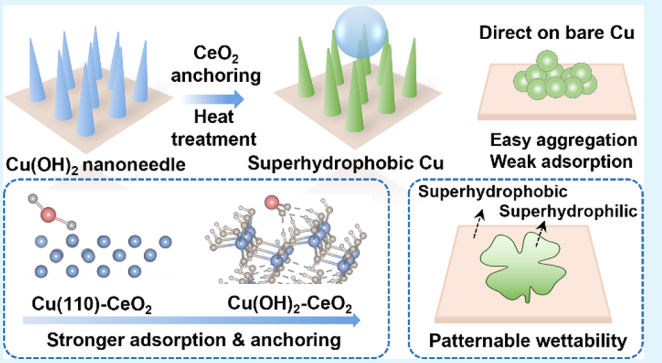

KEYWORDS: *superhydrophobic Cu, CeO_2 electrodeposition, patterned wettability, organic-modifier-free coating, corrosion resistance*

1. INTRODUCTION

Copper and its alloys are widely used in electronic packaging, heat exchange systems and marine engineering due to their excellent electrical and thermal conductivity as well as good machinability.[1−3] However, during actual service, copper surfaces are prone to contamination adhesion and corrosion by chlorine-containing media.[4−6] This results in decreased thermal and electrical transmission efficiency, electrochemical corrosion, and a shortened lifespan of components.[7,8] Therefore, the development of surface protection strategies with integrated water repellency, antifouling, and corrosion resistance is crucial for the long-term stable service of copper materials.[9−11] Inspired by the "lotus leaf effect", superhydrophobic surfaces (SHS) can capture a stable air layer at the solid-liquid interface to inhibit the penetration of corrosive species such as H_2O, O_2, and Cl^-.[12] This mechanism slows down electrochemical reactions and enables self-cleaning properties, making it an ideal protective solution for copper materials.[13,14] Combining micro/nanoscale surface roughness with low-surface-energy chemistry is a widely adopted strategy for constructing superhydrophobic surfaces.[15] The rough structure of the copper substrate can be obtained by various methods such as hydrothermal treatment,[16] electrochemical deposition,[17] and laser[18,19] processing, etc. Subsequently, further modification with low surface energy agents such as fluorosilanes, long-chain fatty acids, or other organic substances is required. However, organic or fluorine-containing modifiers may pose environmental risks, exhibit limited thermal stability, insufficient solvent resistance, and suffer from progressive aging failure under harsh conditions.[20,21] Therefore, the development of SHS that do not require organic post-modification has become an important direction for constructing durable and environmentally friendly protective interfaces for metals.[22]

Received: June 3, 2026
Revised: August 6, 2026
Accepted: August 18, 2026
Published: August 26, 2026

Cerium salts and cerium-based coatings have long been investigated as environmentally benign corrosion inhibitors and alternatives to chromate conversion coatings. Early studies demonstrated the deposition and corrosion-inhibiting effects of cerium oxide/hydroxide species on aluminum alloys.[23] Stoffer and co-workers and O'Keefe co-workers subsequently investigated the formation, surface composition, and corrosion-protection performance of spontaneously deposited and electrodeposited cerium-based conversion coatings.[24,25] Protective cerium oxide/hydroxide layers have also been formed on copper substrates through spontaneous immersion and related processes.[26] These studies established the role of cerium compounds in metal corrosion protection. However, they primarily focused on forming continuous protective or conversion layers rather than simultaneously controlling surface micro/nanostructure and spatial wettability.

Beyond their established role in corrosion protection, rare-earth oxides (REOs), particularly CeO_2, provide an inorganic route for regulating the wettability of metal surfaces.[27,28] Their apparent low surface energy has been associated with both the distinctive electronic structure of REOs and the adsorption/enrichment of nonpolar hydrocarbon species, which together weaken interfacial interactions with water.[28−30] Previous studies have demonstrated the feasibility of constructing superhydrophobic CeO_2-based coatings on metal substrates.[22,31,32] However, direct CeO_2 deposition often relies on random particle aggregation to build surface roughness, resulting in insufficient structural controllability and wetting behavior that is highly dependent on deposition time, coverage, and current density.[33−35] Excessive deposition may also cause particle agglomeration, coating cracking, or substrate exposure. Moreover, most REO-based coatings exhibit globally uniform wettability, making it difficult to fabricate spatially patterned superhydrophilic/superhydrophobic interfaces on a single substrate. A predesigned structural scaffold is therefore desirable to regulate surface roughness and chemistry separately and thereby improve the control of CeO_2 loading and the resulting wetting state.

Herein, we report a strategy for constructing patterned superhydrophobic copper by electrodepositing CeO_2 onto in situ-grown $Cu(OH)_2$ nanoneedle arrays without intentionally added organic or fluorinated modifiers. The $Cu(OH)_2$ nanoneedle array provides a preconstructed one-dimensional rough scaffold and a favorable interface for CeO_2 loading, while CeO_2 deposition introduces additional nanoscale roughness and regulates the surface chemistry. Subsequent vacuum heat treatment promotes surface dehydration and dehydroxylation, accompanied by the relative enrichment of nonpolar hydrocarbon species, thereby decreasing surface polarity and droplet adhesion. A superhydrophobic transition is achieved after heat treatment with a CeO_2 electrodeposition duration as short as 20 s. Patterned superhydrophilic/superhydrophobic regions are further constructed on the same copper substrate through local masking and selective heat treatment. The resulting surfaces exhibit self-cleaning behavior, repellency toward complex liquids, and corrosion protection, and the fabrication strategy can be extended to three-dimensional substrates such as copper mesh and copper foam. This approach integrates controllable micro/nanostructures, wettability regulation, and corrosion protection on a single copper surface and provides a design strategy for multifunctional cerium-based protective interfaces.

2. EXPERIMENTAL SECTION

2.1. Materials

Cu foil was purchased from Kunshan Research Metal Technology Co., Ltd. NaOH was purchased from Anhui Zesheng Technology Co., Ltd. Ammonium persulfate [$(NH_4)_2S_2O_8$], cerium nitrate hexahydrate [$Ce(NO_3)_3{\cdot}6H_2O$], ammonium chloride (NH_4Cl), sulfuric acid (H_2SO_4), potassium chloride (KCl), sodium chloride (NaCl) and ethanol (C_2H_5OH) were purchased from Chengdu Cologne Chemical Co., Ltd.

2.2. Preparation of SHS Cu

Copper foils/meshes/foams were alternately ultrasonically cleaned with deionized water and ethanol to remove contaminants and oil stains. They were then immersed in 0.1 M H_2SO_4 for 60 s to eliminate surface oxides. Subsequently, the copper foils/meshes/foams were immersed in a mixed solution containing 1 M NaOH and 0.05 M $(NH_4)_2S_2O_8$ for 5, 10, 15, and 20 min, respectively, to obtain $Cu(OH)_2$ nanoneedle structures. Using the as-prepared $Cu(OH)_2$ nanoneedle-coated Cu as the working electrode, a Pt electrode as the counter electrode, and an Ag/AgCl (3 M KCl) electrode as the reference electrode, galvanostatic cathodic electrodeposition was performed in 50 mL of an aqueous solution containing 3 mM $Ce(NO_3)_3{\cdot}6H_2O$, 15 mM KCl, and 30 mM NH_4Cl. The electrodeposition was carried out at constant cathodic current densities of −1, −2, and −3 mA cm^{-2} for 30 s, 1 min, 3 min, 5 min, 10 min, and 20 min, at a reaction temperature of 70 °C, yielding CeO_2@$Cu(OH)_2$ deposited samples. Unless otherwise stated, the representative SHS Cu sample was prepared at −1 mA cm^{-2} for 180 s. The obtained samples were further dried in a vacuum drying oven at 120 °C for 4 h to achieve dehydration, thus obtaining superhydrophobic copper surfaces.

2.3. Adsorption Energy Calculation

Density functional theory (DFT) calculations were performed using the Vienna Ab initio Simulation Package (VASP). The exchange-correlation functional was described by the Perdew-Burke-Ernzerhof (PBE) method within the generalized gradient approximation (GGA).[36] The core electrons were represented by the projector augmented-wave (PAW) pseudopotential, while valence electrons were expanded in a plane-wave basis set with a cutoff energy of 500 eV. In all calculations, electronic energy convergence was achieved with a threshold of 10^{-6} eV, and the atomic force threshold was set to 0.02 eV/Å. For slab calculations, a 15 Å vacuum layer was applied along the z-direction. Based on the Monkhorst-Pack scheme, the k-point meshes were set to 2 × 2 × 1 for Cu (110) and 2 × 3 × 1 for $Cu(OH)_2$ (010). The adsorption energy (E_{ad}) was calculated using eq 1:

$$E_{ad} = E_{Sub+Ads} - E_{Sub} - E_{Ads} \quad (1)$$

where $E_{Sub+Ads}$ is the total energy of substrate with adsorbate, E_{Sub} is the energy of bare substrate, and E_{Ads} is the energy of adsorbate, respectively.

2.4. Electrochemical Characterization

Electrochemical potentiodynamic polarization and electrochemical impedance spectroscopy (EIS) measurements were conducted on copper foils using an electrochemical workstation (Gamry Interface 1010E), with all tests performed in 3.5 wt % NaCl solution. A standard three-electrode system was adopted, in which a platinum electrode served as the counter electrode, a saturated calomel electrode (SCE) as the reference electrode, and the copper foil as the working electrode. Prior to testing, each sample was immersed in the electrolyte for 30 min to stabilize the open circuit potential (E_{ocp}). The EIS tests were implemented over a frequency range of 10^5–10^{-2} Hz with an AC amplitude of 5 mV. The potentiodynamic polarization curves were scanned from −250 mV to +250 mV relative to E_{ocp} at a scan rate of

https://doi.org/10.1021/acsami.6c11391
ACS Appl. Mater. Interfaces 2026, 18, 48405−48416

1 mV·s^{-1}. The corrosion inhibition efficiency (η) was calculated according to eq 2.

$$\eta\% = \frac{i^0_{corr} - i_{corr}}{i^0_{corr}} \times 100\% \quad (2)$$

where i^0_{corr} refers to the corrosion current density of pristine copper foil, i_{corr} refers to that of SHS Cu.

2.5. Characterization

Scanning electron microscopy (SEM) images and energy dispersive spectroscopy (EDS) maps were acquired using a Sigma 360 (Zeiss, Germany). X-ray photoelectron spectroscopy (XPS) tests were conducted by K-Alpha (Thermo Scientific, USA). Surface adhesion force and droplet rebound experiments were measured with an LSA100S-T contact angle/surface tension tester (LAUDA·Scientific, Germany). The contact angle (CA) and sliding angle (SA) of the samples were determined via a JY-PHb contact angle measuring instrument. Three distinct positions on each sample were tested for CA and SA characterization, with droplet volumes set to 3 μL and 10 μL for CA and SA measurements, respectively. High-Resolution transmission electron microscopy (HRTEM) data were collected using a JEM-F200 device (JEOL, Japan). Three-dimensional surface topographies were obtained using a three-dimensional laser scanning confocal microscope (VK-X150, Keyence, Japan). Thermogravimetric analysis (TGA) was performed using a PE STA 9 thermal analyzer. Samples with dimensions of 1.0 cm × 1.0 cm were heated from 35 to 300 °C at a heating rate of 5 °C min^{-1} under an argon atmosphere.

3. RESULTS AND DISCUSSION

3.1. Construction and Structural Characterization of SHS Cu

As shown in Figure 1a, a three-step strategy involving chemical oxidation, electrochemical deposition, and vacuum heat treatment was employed to construct SHS on a copper substrate. First, a $Cu(OH)_2$ nanoneedle array was grown in situ on the bare Cu substrate through alkaline oxidation. The array served as a preconstructed structural scaffold and interfacial support for subsequent CeO_2 loading. Subsequently, CeO_2 was approximately uniformly deposited onto the $Cu(OH)_2$ nanoneedles via electrochemical deposition, successfully constructing CeO_2@$Cu(OH)_2$ composite nanoneedle structures. A representative potential-time curve recorded at −1 mA cm^{-2} for 180 s exhibited a brief initial transient, after which the potential stabilized at approximately −0.16 V vs Ag/AgCl (Figure S1), indicating a relatively stable cathodic deposition process. Under cathodic polarization, reduction reactions involving nitrate ions and dissolved oxygen near the working electrode can generate OH^-, thereby increasing the local pH at the electrode/electrolyte interface. The locally generated OH^- promotes the hydrolysis and precipitation of Ce^{3+} species to form a $Ce(OH)_3$-type precursor, which is subsequently oxidized and dehydrated to form CeO_2.[37,38] Finally, a vacuum heat treatment process at 120 °C was applied, successfully producing SHS Cu without intentionally added organic low-surface-energy modifiers while preserving the integrity of the desired nanoneedle structure.

To compare the interfacial affinity of CeO_2 toward Cu and $Cu(OH)_2$, adsorption models of CeO_2 on Cu(110) and $Cu(OH)_2$(010) were constructed. The corresponding top and side views are shown in Figure 1b,c respectively. The adsorption energy (E_{ad}) of CeO_2 was −2.12 eV on Cu(110) and −2.33 eV on $Cu(OH)_2$(010). Within the models considered, the more negative E_{ad} of CeO_2 on $Cu(OH)_2$(010) indicates thermodynamically more favorable interfacial adsorption. This result provides energetic support for the possibility that the $Cu(OH)_2$ nanoneedle array offers a favorable interface for CeO_2 loading.

Figure 1d summarizes the evolution of surface wettability throughout the fabrication process. The pristine bare copper exhibited intrinsic hydrophilicity with a water contact angle (WCA) of 80.2°. Although the $Cu(OH)_2$ nanoneedle array greatly increased surface roughness, the surface was rich in polar hydroxyl groups (−OH). According to the Wenzel wetting model,[39,40] the increase in surface roughness amplifies the inherent wettability, thereby rendering the $Cu(OH)_2$ nanoneedle surface superhydrophilic with a WCA decreasing to 0°. Vacuum heating of the $Cu(OH)_2$ nanoneedles without CeO_2 deposition increased the WCA to 130.1°. However, the water droplet remained strongly pinned during contact and retraction, as further demonstrated by the dynamic adhesion test (Figure S7 and Movie S1), indicating a hydrophobic but highly adhesive wetting state. The as-electrodeposited CeO_2@$Cu(OH)_2$ surface also exhibited a WCA of 0°, which can be attributed to the adsorbed water and residual hydroxylated species associated with the aqueous electrodeposition process. After subsequent vacuum heating, the WCA increased to 157.6°, and the water droplet maintained an almost spherical shape, demonstrating that the fabricated surface achieves a stable Cassie−Baxter non-wetting state.[41,42] Under identical vacuum heat-treatment conditions, the $Cu(OH)_2$ nanoneedle surface without CeO_2 deposition exhibited only a highly adhesive hydrophobic state, whereas the CeO_2-deposited sample became superhydrophobic, indicating that the introduction of CeO_2 is a key factor in achieving this superhydrophobic transition.

The evolution of the surface microstructure serves as the physical foundation for achieving wettability transition. The bare Cu surface was relatively smooth, with an arithmetic mean height (S_a) of 0.345 μm (Figure 2a,e). After alkaline oxidation, $Cu(OH)_2$ nanoneedles progressively developed on the Cu surface with increasing reaction time.[43,44] In the strongly alkaline $NaOH/(NH_4)_2S_2O_8$ solution, $S_2O_8^{2-}$ primarily acts as an oxidant, promoting the oxidation of Cu^0 at the Cu/solution interface and the formation of Cu(II)-containing species, which subsequently react with OH^- to form $Cu(OH)_2$ nuclei.[45] Continued interfacial oxidation and anisotropic growth further promote the elongation and densification of the $Cu(OH)_2$ nanoneedles with increasing reaction time. The relatively sparse, short bud-like structures observed after 5 min correspond to an early nucleation-and-growth stage, with an S_a of 0.726 μm (Figure S2a,d). When the oxidation time was extended to 10 and 15 min, the nanoneedles became progressively longer and more densely distributed (Figure S2b,c). The corresponding S_a values increased to 1.015 and 1.201 μm, respectively (Figure S2e,f). After 20 min, a dense and relatively uniform $Cu(OH)_2$ nanoneedle array was formed on the Cu surface (Figure 2b), and S_a further increased to 1.355 μm (Figure 2f). After CeO_2 electrodeposition, the original nanoneedle framework remained intact, while S_a increased from 1.355 to 2.297 μm (Figure 2c,g). Following subsequent vacuum heat treatment, the overall nanoneedle morphology remained well preserved (Figure 2d), and S_a changed only slightly from 2.297 to 2.328 μm (Figure 2h), indicating that

https://doi.org/10.1021/acsami.6c11391
ACS Appl. Mater. Interfaces 2026, 18, 48405−48416

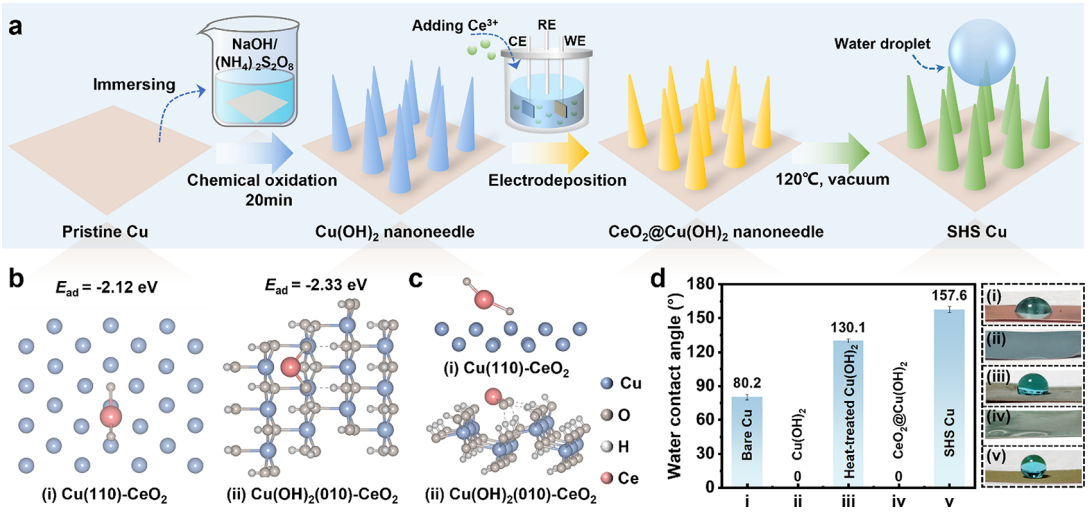

Figure 1. Fabrication and wettability evolution of SHS Cu. (a) Schematic illustration of the fabrication process of SHS Cu. (b) Top and (c) side views of the optimized adsorption configurations of CeO_2 on (i) Cu(110) and (ii) $Cu(OH)_2$(010), with the corresponding adsorption energies shown in panel (b). (d) WCAs and representative droplet photographs of (i) bare Cu, (ii) $Cu(OH)_2$ nanoneedle array, (iii) heat-treated $Cu(OH)_2$ nanoneedle array without CeO_2 deposition, (iv) CeO_2@$Cu(OH)_2$ nanoneedle array, and (v) SHS Cu.

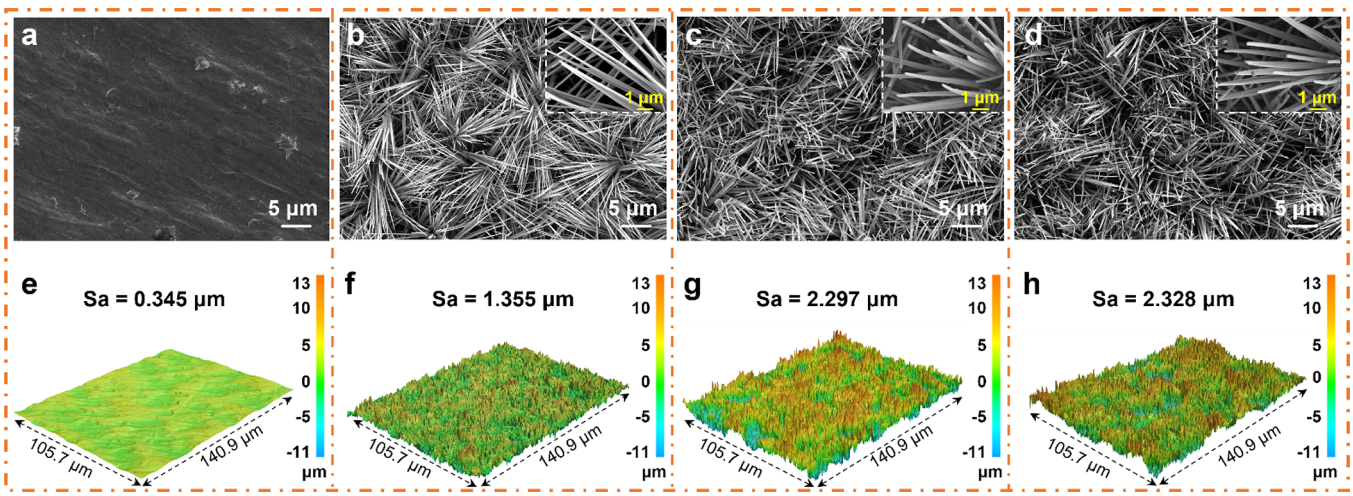

Figure 2. Morphological and surface roughness evolution during the fabrication of SHS Cu. (a–d) SEM images and (e–h) corresponding three-dimensional surface topographies of Cu at different processing stages: (a, e) bare Cu, (b, f) $Cu(OH)_2$ nanoneedles, (c, g) CeO_2@$Cu(OH)_2$, and (d, h) SHS Cu.

vacuum heat treatment did not cause pronounced reconstruction of the surface morphology. The increased roughness after CeO_2 electrodeposition demonstrates that CeO_2 introduces additional surface roughness while preserving the original $Cu(OH)_2$ nanoneedle framework. This additional roughness provides an important structural contribution to the transition from the highly adhesive hydrophobic state of heat-treated $Cu(OH)_2$ to the low-adhesion superhydrophobic state of the CeO_2@$Cu(OH)_2$ surface after vacuum heat treatment.

For the chemically oxidized Cu sample without CeO_2 deposition (0 min), the XRD pattern displays not only the strong characteristic diffraction peaks of the Cu substrate (PDF#70–3038) but also several distinct diffraction peaks assigned to $Cu(OH)_2$ (PDF #80-0656), confirming the successful formation of $Cu(OH)_2$ nanoneedles on the Cu surface (Figure 3a). Following CeO_2 electrodeposition and subsequent heat treatment, a new diffraction peak corresponding to the CeO_2 (111) plane appears at 28.78° (PDF #81-0792). The peak intensity gradually increases with prolonged deposition time, directly indicating a continuous rise in the loading amount of CeO_2. The broadening of the CeO_2 diffraction peak reveals that the deposited ceria possesses a nanoscale crystalline size. Meanwhile, new characteristic diffraction peaks of Cu_2O (111) and Cu_2O (220) emerge on the superhydrophobic copper surface after heat treatment (PDF #77-0199). Owing to the X-ray shielding effect of the gradually thickened surface CeO_2 layer and the partial consumption of $Cu(OH)_2$ during thermal treatment, the characteristic peak intensities of both $Cu(OH)_2$ and Cu_2O exhibit a regular relative attenuation trend as the deposition time increases.

To determine the elemental composition and chemical states of the surface, XPS analyses were performed on copper

https://doi.org/10.1021/acsami.6c11391
ACS Appl. Mater. Interfaces 2026, 18, 48405–48416

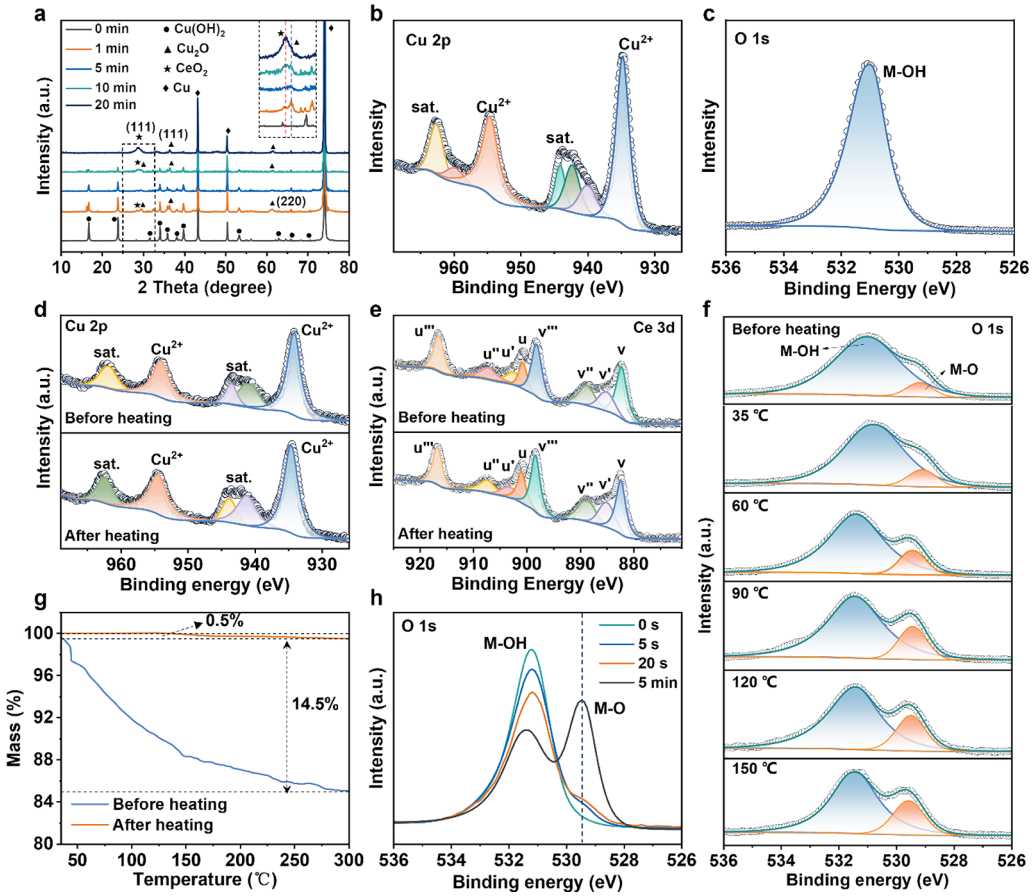

Figure 3. (a) XRD patterns of $Cu(OH)_2$ nanoneedles after CeO_2 deposition for different durations (0, 1, 5, 10, and 20 min). (b) Cu 2p and (c) O 1s XPS spectra of $Cu(OH)_2$ nanoneedles. (d) Cu 2p and (e) Ce 3d XPS spectra of CeO_2@$Cu(OH)_2$ and SHS Cu. (f) O 1s XPS spectra of the CeO_2@$Cu(OH)_2$ samples before heating and after vacuum heating at 35, 60, 90, 120, and 150 °C for 4 h. (g) Thermogravimetric curves of the CeO_2@$Cu(OH)_2$ samples before and after vacuum heat treatment. (h) O 1s XPS spectra of SHS Cu samples prepared with different CeO_2 electrodeposition durations.

samples at different preparation stages. In the Cu 2p spectrum, two prominent peaks observed at 934.78 eV and 954.68 eV correspond to Cu $2p_{3/2}$ and Cu $2p_{1/2}$,[46] respectively (Figure 3b). Intense shake-up satellite peaks appear on the high-binding-energy side of the main peaks, which are characteristic of divalent copper (Cu^{2+}).[47] In addition, the O 1s spectrum (Figure 3c) presents a single symmetric peak at 531.08 eV, corresponding to metal-coordinated hydroxyl groups (M−OH), indicating that alkaline etching promoted the in situ growth of high-purity $Cu(OH)_2$ crystal phases on the bare Cu surface.[46] After the electrochemical deposition of CeO_2, the Cu 2p spectrum of the sample still retains the characteristic satellite peaks of Cu^{2+} (Figure 3d), indicating that copper species on the surface mainly exist in the divalent state. The Ce 3d spectra of the samples before and after heat treatment can both be fitted into typical multiplet splitting peaks of Ce^{4+} (v, v″, v‴ and u, u″, u‴) together with faint Ce^{3+} peaks (v′, u′), indicating the presence of trace amounts of Ce^{3+} species in the deposited CeO_2 layer[27,48] (Figure 3e). The chemical state of Ce remains highly consistent before and after heat treatment, demonstrating no pronounced change in the Ce oxidation-state distribution.

To further examine the effect of thermal treatment on the surface oxygen species, O 1s XPS spectra were collected from CeO_2@$Cu(OH)_2$ samples prepared with a CeO_2 electrodeposition time of 3 min and subsequently heated at different temperatures (Figure 3f). Compared with the $Cu(OH)_2$ nanoneedles, the O 1s spectra of CeO_2@$Cu(OH)_2$ were deconvoluted into metal−oxygen (M−O) and hydroxyl oxygen (M−OH) components.[22] As the heating temperature increased, the relative contribution of M−O increased, and the M−O/M−OH peak-area ratio increased from 0.111 for the unheated CeO_2@$Cu(OH)_2$ to 0.342 after heating at 150 °C (Figure S3a). The evolution of the surface oxygen species was accompanied by a corresponding change in wettability. The unheated CeO_2@$Cu(OH)_2$ was completely wetted by water. After heating at 35 °C, the surface remained hydrophilic, with a WCA of 26.7°. The surface became hydrophobic after heating at 60 °C, with a WCA of 99.8°. At 90 °C and above, the samples became superhydrophobic, with WCAs exceeding 150° (Figure S3b). The concurrent evolution of the surface oxygen species and wettability indicates that the progressive removal of hydroxyl species during heating reduces the affinity of the surface for water. Thermogravimetric analysis further showed that the unheated sample exhibited a mass loss of approximately 14.5% over the temperature range of 35–300 °C, whereas the sample pretreated at 120 °C for 4 h showed a mass loss of only approximately 0.5% over the same temperature range

https://doi.org/10.1021/acsami.6c11391
ACS Appl. Mater. Interfaces 2026, 18, 48405−48416

(Figure 3g). These results are consistent with the removal of adsorbed water and thermally labile hydroxyl-containing species during vacuum heating. The progressive dehydration and dehydroxylation reduce the polar character of the surface and promote the transition toward a hydrophobic state.

The origin of the M−O component was further examined by comparing the O 1s XPS spectra of samples prepared using different CeO_2 electrodeposition durations and subjected to the same heat treatment (Figure 3h). The heat-treated $Cu(OH)_2$ sample without CeO_2 deposition remained dominated by the M−OH component, with no clearly resolved M−O component. A weak M−O component appeared after CeO_2 electrodeposition for 5 s and gradually increased with electrodeposition duration. This trend indicates that the enhanced M−O contribution is primarily associated with Ce−O lattice oxygen in the deposited CeO_2.

In addition to the changes in surface hydroxylation, the C 1s spectra provide complementary information on the surface carbon species associated with the wettability transition. Although no organic or fluorinated modifier was intentionally introduced during fabrication, C−C/C−H, C−O, and O−C═O components were detected in the C 1s spectra (Figure S4a). These components are attributed to adventitious carbon arising from the passive adsorption of trace volatile organic species from the conventional vacuum environment and during unavoidable sample handling, rather than from a deliberately applied hydrocarbon treatment. After heat treatment, the relative contribution of the C−C/C−H component increased, while that of oxygen-containing carbon species decreased, indicating that the outermost surface became more enriched with nonpolar carbonaceous species.[49] Consistently, the C 1s spectra of samples with different CeO_2 deposition durations show an enhanced C−C/C−H signal with increasing deposition time (Figure S4b), suggesting that the CeO_2-modified surface is more favorable for the adsorption/enrichment of hydrocarbon species. Previous studies have shown that rare-earth-oxide surfaces are able to adsorb hydrocarbon species, and the adsorbed nonpolar C−C/C−H groups can lower the surface free energy, thereby enhancing the apparent hydrophobicity of oxide surfaces.[29,30] The quantitative results summarized in Table S1 also support this trend, showing increased C/(Cu + Ce) and C−C/C−H-related ratios after heat treatment. These results indicate that the heat-treated CeO_2@$Cu(OH)_2$ surface possesses fewer polar hydroxyl groups and a higher proportion of nonpolar carbonaceous species, both of which contribute to the reduction of surface free energy and the formation of superhydrophobicity.

The SEM and TEM results clearly reveal the microstructural evolution of the samples during alkaline etching and subsequent CeO_2 electrodeposition. As illustrated in Figure 4a,b, the Cu sample after alkaline etching exhibits a regular one-dimensional (1D) nanoneedle morphology. The corresponding HRTEM image shows distinguishable lattice fringes of 0.257 nm and 0.229 nm, which correspond to the (002) and (130) crystal planes of $Cu(OH)_2$, respectively (Figure 4c). The selected area electron diffraction (SAED) pattern matches the diffraction characteristics of $Cu(OH)_2$ (Figure 4d). Elemental distribution mapping further demonstrates the uniform dispersion of Cu and O across the nanoneedles, confirming the formation of well-crystallized 1D $Cu(OH)_2$ nanoneedles on the Cu surface after alkaline etching (Figure 4e).

After CeO_2 electrodeposition for 3 min, the average diameter of the nanoneedles increased from 115.06 nm to 161.41 nm (Figure 4f,g). New lattice spacings of 0.304 nm and 0.307 nm appear in the HRTEM images, which are highly consistent with the CeO_2 (111) plane (Figure 4h). The SAED pattern presents distinct diffraction rings corresponding to the (111), (200), (311) planes of CeO_2 and (002) plane of $Cu(OH)_2$ (Figure 4i). Elemental mapping further showed that Ce was uniformly distributed along the nanoneedle surface (Figure 4j). Collectively, the HRTEM, SAED, and elemental-mapping results demonstrate the successful formation of a uniformly distributed polycrystalline CeO_2 deposit on the $Cu(OH)_2$ nanoneedles.

When the deposition time was extended to 20 min, the nanoneedle diameter further increased to 261.36 nm (Figure 4k,l), suggesting continuous deposition and remarkable thickening of the CeO_2 layer. At this stage, the HRTEM image retains the 0.304 nm fringe associated with the CeO_2 (111) plane and exhibits an additional 0.267 nm fringe corresponding to the CeO_2 (200) (Figure 4m). Furthermore, the SAED pattern displays additional diffraction rings of the CeO_2 (331) plane, suggesting an enhanced crystallinity of the deposited CeO_2 (Figure 4n). Elemental distribution mapping reveals that the spatial distribution of Ce remains homogeneous within the nanoneedle region as the deposition time increases (Figure 4o). Furthermore, EDS mapping analyses of the copper after 3 min and 20 min of CeO_2 deposition also demonstrate a uniform distribution of Ce, Cu, and O elements in the regions containing the 1D nanoneedles (Figure S5a,b). Notably, the atomic proportion of Ce increased with longer deposition times. Overall, the electrodeposition process enables the gradual growth of CeO_2 on the $Cu(OH)_2$ surface while maintaining the integrity of the 1D nanoneedle skeleton. This development lays the groundwork for the construction of composite micro-nanostructures and the utilization of rare earth oxides with superhydrophobic properties.

The deposition morphology of CeO_2 on the $Cu(OH)_2$ nanoneedle arrays exhibited a significant current-dependent behavior at varying current densities. At a low current density of −1 mA cm^{-2}, the pristine nanoneedle structure of the $Cu(OH)_2$ was maintained, with only slight surface roughening observed (Figure S6a). This indicates that CeO_2 was uniformly anchored onto the nanoneedle surfaces primarily in the form of thin coatings or fine nanoparticles. As the current density was increased to −2 mA cm^{-2}, the CeO_2 deposition layer on the nanoneedle surfaces thickened noticeably, whereas the overall 1D structure was still well preserved (Figure S6b). This suggests that heterogeneous nucleation and subsequent growth of CeO_2 were promoted under this condition, without severe particle agglomeration occurring. When the current density was further increased to −3 mA cm^{-2}, massive particulate and cluster-like deposits emerged on the nanoneedle surfaces, accompanied by bridging and accumulation in localized regions (Figure S6c). This demonstrates that an excessively high current density triggers the rapid formation of numerous CeO_2 nanoparticles near the electrode surface and their subsequent agglomeration. Accordingly, a relatively low current density is conducive to the fabrication of a uniform CeO_2 modification layer. By contrast, a high current density switched the dominant deposition mechanism from surface heterogeneous nucleation to rapid precipitation and particle agglomeration.

https://doi.org/10.1021/acsami.6c11391
ACS Appl. Mater. Interfaces 2026, 18, 48405−48416

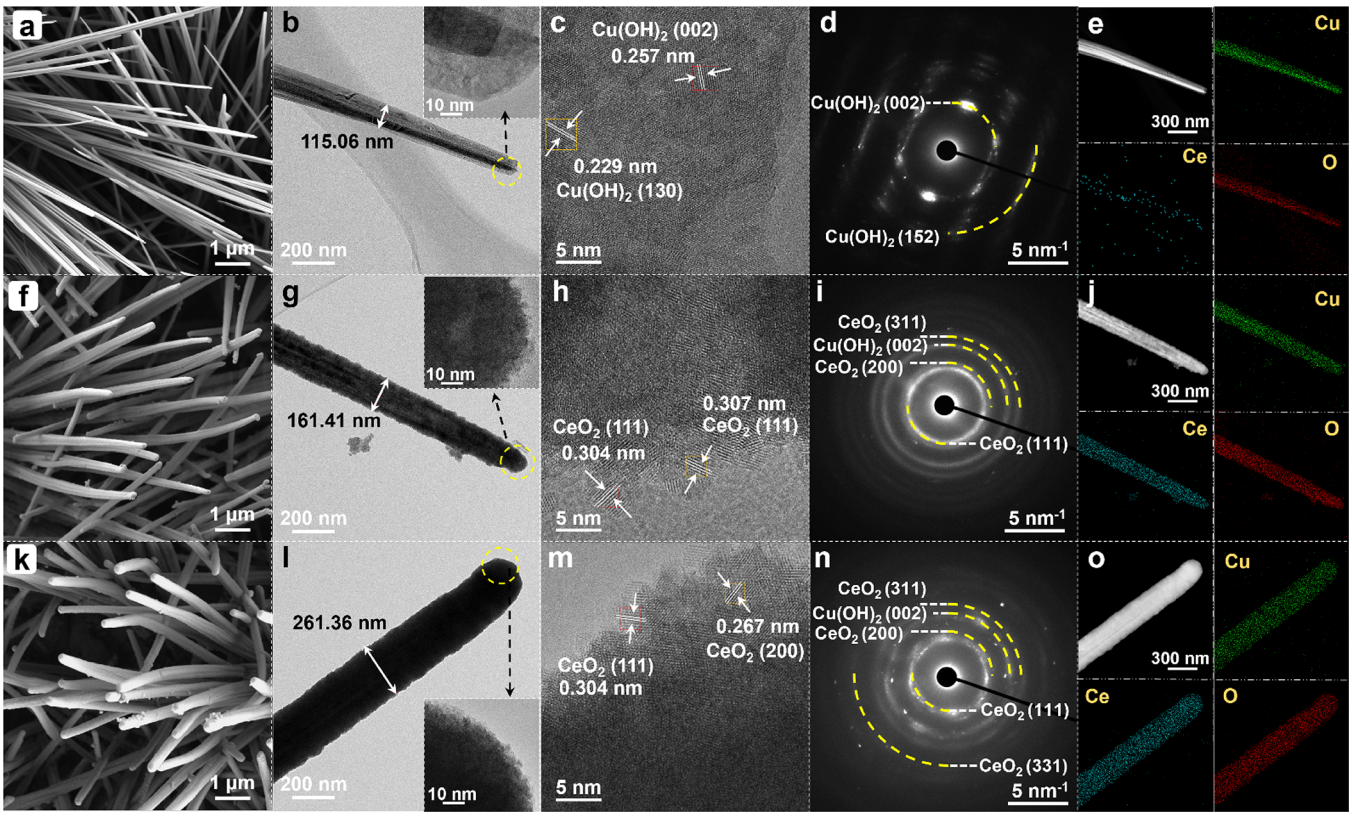

Figure 4. (a–e) $Cu(OH)_2$ nanoneedles: (a) SEM, (b) TEM, (c) HRTEM, (d) SAED, and (e) elemental mapping images. (f–j) SHS Cu after depositing CeO_2 for 3 min: (f) SEM, (g) TEM, (h) HRTEM, (i) SAED, and (j) elemental mapping images. (k–o) SHS Cu after depositing CeO_2 for 20 min: (k) SEM, (l) TEM, (m) HRTEM, (n) SAED, and (o) elemental mapping images.

3.2. Surface Wettability and Chemical Stability Analysis

To systematically evaluate the superhydrophobic performance of copper surfaces after CeO_2 electrodeposition, both static and dynamic wetting behaviors were characterized. As illustrated in Figure 5a, the copper surface exhibited stable superhydrophobicity after CeO_2 electrodeposition and subsequent vacuum heat treatment. The heat-treated $Cu(OH)_2$ nanoneedle surface without CeO_2 deposition exhibited a WCA of 130.1° and the droplet was pinned on the surface rather than easily rolling off. This result is further confirmed by the dynamic water adhesion test in Figure S7, where the water droplet remained attached to the heat-treated $Cu(OH)_2$ surface during contact and retraction (Movie S1). Therefore, the thermally treated $Cu(OH)_2$ nanoneedle array alone can only produce a hydrophobic but highly adhesive surface, which is insufficient for achieving a stable low-adhesion superhydrophobic state. When the electrodeposition time was increased from 20 s to 300 s, the static WCA remained above 152°, while the SA stayed below 5°, indicating that the introduction of CeO_2 rapidly converted the high-adhesion hydrophobic $Cu(OH)_2$ surface into a low-adhesion superhydrophobic surface and that the surface wetting behavior became relatively insensitive to further increases in electrodeposition time. This stability can be attributed to the in situ formation of $Cu(OH)_2$ nanoneedles during alkaline oxidation, which provides the essential roughness for achieving superhydrophobicity. The $Cu(OH)_2$ nanoneedle array provides the primary rough framework, while CeO_2 deposition introduces additional nanoscale roughness and modifies the surface chemistry. Thus, a short CeO_2 electrodeposition time is sufficient to endow the pre-roughened substrate with a superhydrophobic state, eliminating the requirement for prolonged deposition to optimize surface morphology.

To further quantify the interaction at the solid–liquid interface, dynamic adhesion force measurements (Figure 5b) were conducted, revealing that the maximum tensile adhesion force of a water droplet during contact and retraction from the surface was only 21.4 μN. Such an extremely low interfacial adhesion force demonstrates the outstanding water repellency of the SHS Cu. Furthermore, the WCAs of droplets with different pH values on the sample surface all exceed 150° (Figure 5c), and they can easily roll off the sample surface (Figure S8). After immersion in sodium chloride solutions with various mass fractions for 24 h, the sample still maintained a superhydrophobic state with a static WCA above 150°, confirming the favorable chemical stability of the as-prepared SHS Cu (Figure 5d). The mechanical durability of SHS Cu was further evaluated through repeated droplet-impact, tape-peeling, and cyclic bending tests (Figure 5e–g). During the droplet-impact test, water droplets were released at a dispensing rate of 35 μL s^{-1} from a height of 2.5 cm onto the same area of the sample surface. After 1000 consecutive impacts, the water contact angle remained approximately 154°. For the tape-peeling test, a polyimide pressure-sensitive adhesive tape was applied to the same surface area under a pressure of 50 kPa for 5 s before being peeled off, with a fresh tape or unused adhesive area employed for each cycle. After 300 peeling cycles, the water contact angle decreased from 156.3° to 152.7° but remained above 150°. In

https://doi.org/10.1021/acsami.6c11391
ACS Appl. Mater. Interfaces 2026, 18, 48405–48416

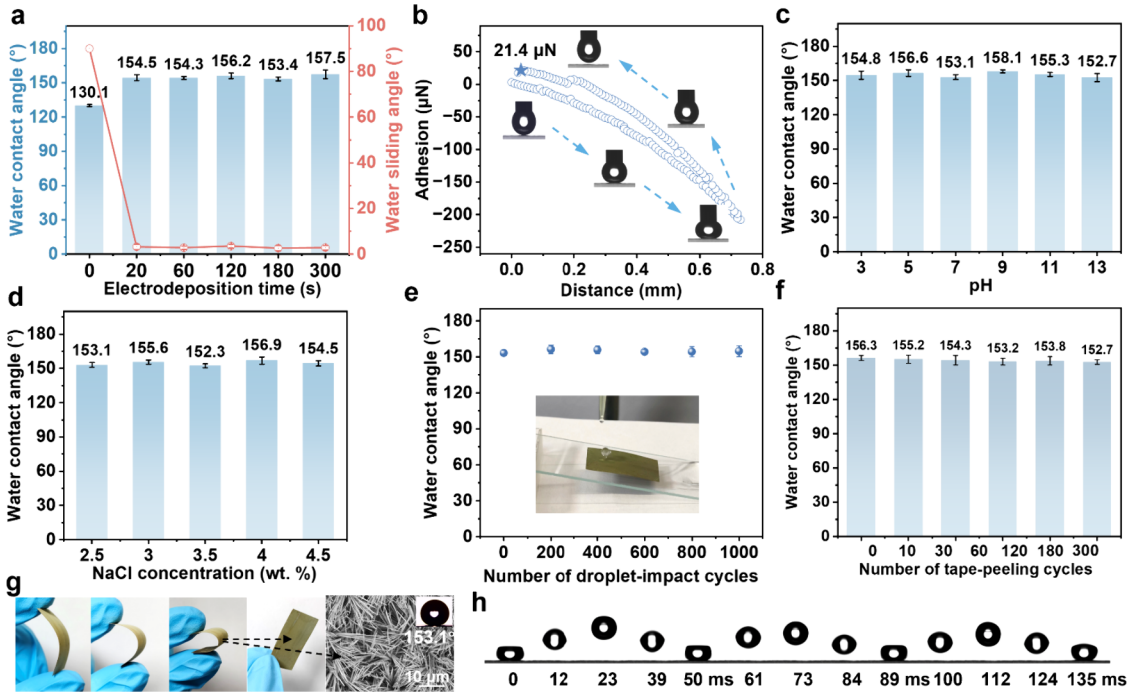

Figure 5. Characterization of surface wettability and chemical stability of SHS Cu. (a) Effect of CeO_2 electrodeposition time on WCA and SA of copper surfaces. (b) Dynamic adhesion force-distance curve of water droplets on the SHS Cu. (c) CA of liquids with different pH values on the SHS Cu. (d) WCA of SHS Cu after immersion in NaCl solutions with different mass fractions for 24 h. (e) Water contact angles of SHS Cu after repeated droplet-impact cycles. (f) Water contact angles of SHS Cu after repeated tape-peeling cycles. (g) Photographs of SHS Cu during the cyclic bending test and the corresponding SEM image after 50 bending cycles. (h) Continuous bouncing process of water droplets on the SHS Cu.

the cyclic bending test, the two ends of the sample were bent toward each other until they became parallel and then released to restore the sample to a flat state. After 50 bending cycles, no obvious permanent creases or macroscopic surface delamination were observed. SEM examination of the region subjected to the maximum curvature revealed no apparent cracking, delamination, or collapse of the nanoneedle array, and the WCA in this region remained at 153.1°. These results demonstrate that SHS Cu retained a high static water contact angle and a certain degree of structural integrity under the tested mechanical conditions. Figure 5h presents the impact behavior of water droplets on the SHS. Upon contacting the surface, the water droplet rebounded rapidly and underwent continuous bouncing without obvious pinning or liquid residue (Movie S2), verifying the extremely low contact angle hysteresis and superior dynamic water-repellent performance of the surface.

3.3. Fabrication of Patterned Superhydrophobic/Superhydrophilic Copper Surfaces

A patterned surface with coexisting superhydrophilic and superhydrophobic wettability was constructed on copper via a selective heat treatment strategy. Prior to heat treatment at 120 °C, a shadow mask with a specific shape was closely attached to the electrodeposited CeO_2@$Cu(OH)_2$ surface. The masked regions retained the original superhydrophilicity, while the exposed regions were converted to a superhydrophobic state after heat treatment, thereby forming well-defined wettability patterns (Figure 6a). O 1s XPS spectra acquired from two different regions on the same sample reveal distinct differences in their surface chemical states (Figure 6b). The superhydrophilic region is dominated by high-binding-energy M−OH

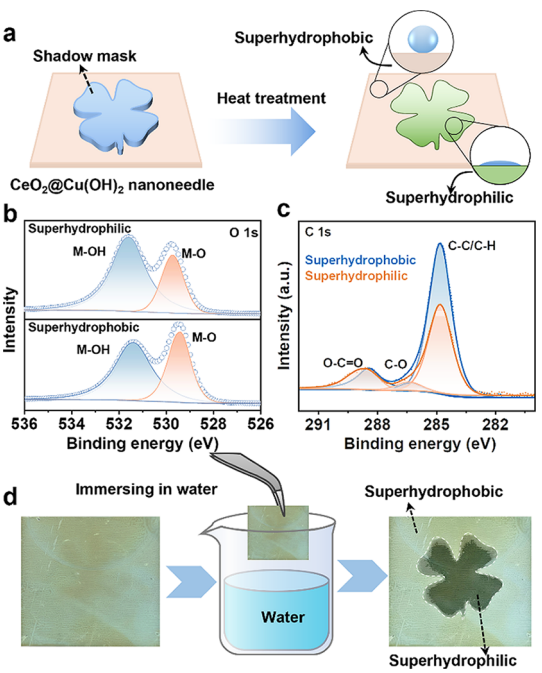

Figure 6. Fabrication and characterization of patterned SHS Cu. (a) Schematic illustration of the fabrication of patterned superhydrophobic/superhydrophilic surfaces via a masking method combined with heat treatment. (b) O 1s and (c) C 1s XPS spectra acquired from the superhydrophilic and superhydrophobic regions of a patterned sample prepared with a CeO_2 electrodeposition time of 5 min. (d) Macroscopic optical photographs of the sample before and after water immersion, demonstrating the patterned wettability difference.

https://doi.org/10.1021/acsami.6c11391
ACS Appl. Mater. Interfaces 2026, 18, 48405−48416

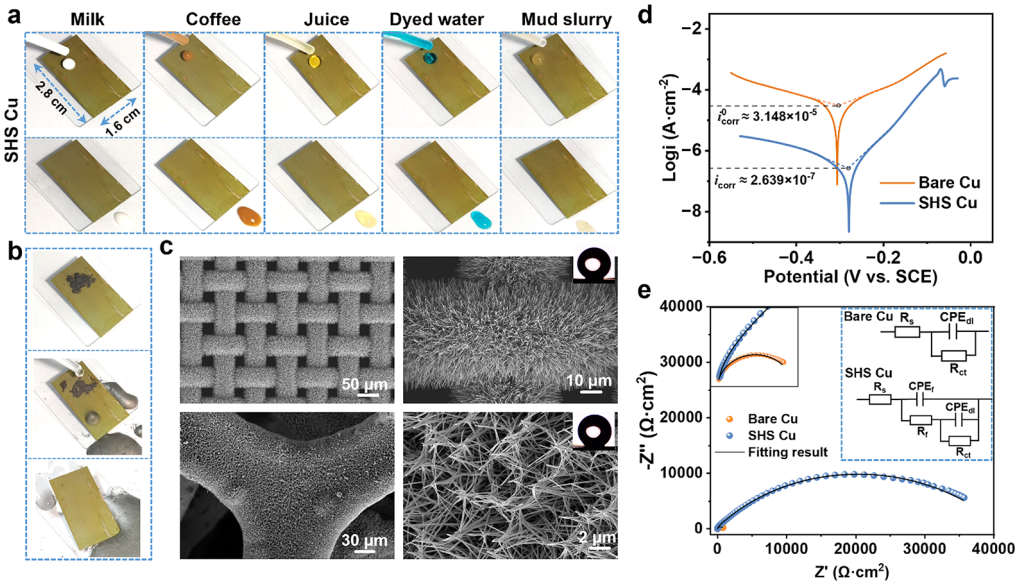

Figure 7. Self-cleaning, substrate universality, and corrosion resistance of the SHS Cu. (a) Sliding behavior of various liquids (milk, coffee, juice, dyed water, and mud slurry) on SHS Cu. (b) Self-cleaning test. The Cu foil size was 2.8 cm × 1.6 cm. (c) SEM images of SHS Cu fabricated on copper mesh and copper foam substrates. (d) Potentiodynamic polarization curves. i^0_{corr} and i_{corr} denote the corrosion current densities of bare Cu and SHS Cu, respectively. (e) Nyquist plots and corresponding equivalent circuit diagram of bare Cu and SHS Cu.

components, indicating a rich population of hydroxyl groups that enhance interaction with water molecules and promote droplet spreading in the masked region. In contrast, the peak intensity of low-binding-energy lattice M-O increases significantly in the superhydrophobic region, accompanied by a weakened M−OH peak. This demonstrates that heat treatment effectively reduces the surface hydroxyl content and induces surface dehydroxylation in the exposed region. The reduction in polar hydroxyl sites, combined with the inherent rough structure of the CeO_2@$Cu(OH)_2$ nanoneedles, enables the wettability transition of exposed areas from superhydrophilicity to superhydrophobicity.

The C 1s spectra further support the chemical difference between the superhydrophilic and superhydrophobic regions (Figure 6c). Compared with the superhydrophilic region, the superhydrophobic region exhibits a higher relative contribution of nonpolar C−C/C−H species, whereas the oxygen-containing carbon components, including C−O and O−C═O, are relatively weakened.[49] This result indicates that the selectively heated region not only undergoes dehydroxylation but also possesses a more nonpolar carbonaceous outermost surface. Such enrichment of hydrocarbon-like species further reduces the surface free energy and cooperates with the micro/nano roughness of the CeO_2@$Cu(OH)_2$ nanoneedles to stabilize the superhydrophobic state. By contrast, the masked region preserves more polar hydroxyl/oxygen-containing species, allowing water to spread rapidly and maintain superhydrophilicity.

Water immersion experiments further visually verify the successful fabrication of the patterned surface. After the patterned sample was fully immersed in water and subsequently taken out, distinguishable wettability differences were observed (Figure 6d and Movie S3). The regions shielded by the four-leaf clover mask presented a dark tone due to thorough wetting, forming a distinct four-leaf clover outline. By comparison, the exposed regions exhibited superhydrophobicity due to the prior heat treatment and showed no water residue after immersion. The above results confirm that patterned wettability interfaces can be fabricated through selective dehydroxylation and localized regulation of surface carbonaceous species using this strategy. This approach requires no additional chemical modification or sophisticated lithography processes, holding promising application potential in microfluidic control, droplet manipulation, and atmospheric water harvesting, among other fields.

3.4. Self-Cleaning, Substrate Universality, and Anti-Corrosion Performance

Copper surfaces are highly prone to reduced electrical conductivity, localized corrosion, and the formation of insulating layers due to the adhesion of contaminants, thereby increasing contact resistance. This not only hinders electron transport but also may lead to the functional failure of key electronic components. Biomimetic SHS can enable contaminating liquids to form spherical droplets that slide off rapidly, while removing solid contaminants through the mechanical action of rolling water droplets, thus achieving excellent self-cleaning capability. To evaluate the practical application potential of SHS Cu, its anti-fouling performance against various daily liquids and self-cleaning ability for solid powders were tested. As shown in Figure 7a, test droplets with different properties, including milk, coffee, fruit juice, dyed water, and mud slurry, maintained nearly spherical shapes upon contact with the SHS Cu and quickly rolled off without leaving any wetting traces (Movie S4). When graphite powder was used to simulate solid contaminants, water droplets rolling off the inclined SHS Cu surface effectively carried away the graphite powder under the influence

Table 1. Polarization Curve Parameters of the Bare Cu and SHS Cu in 3.5 wt % NaCl Solution

samples	E_{corr} (V vs SCE)	I_{corr} (A·cm^{-2})	η (%)
bare Cu	−0.301	3.148×10^{-5}	
SHS Cu	−0.279	2.639×10^{-7}	99.162

https://doi.org/10.1021/acsami.6c11391
ACS Appl. Mater. Interfaces 2026, 18, 48405−48416

Table 2. EIS Fitting Parameters of Bare Cu and SHS Cu in 3.5 wt % NaCl Solution

	R_s [Ω·cm^2]	CPE$_f$ [Ω^{-1}·cm^{-2}·s^n]	n_f	R_f [Ω·cm^2]	CPE$_{dl}$ [Ω^{-1}·cm^{-2}·s^n]	n$_{dl}$	R_{ct} [Ω·cm^2]
bare Cu	4.858				1.767×10^{-4}	0.8127	9.217×10^2
SHS Cu	8.269	1.506×10^{-7}	0.914	1162	5.035×10^{-6}	0.549	4.013×10^4

of gravity, thoroughly cleaning the surface without leaving any residue (Figure 7b). This indicates that the surface exhibits excellent low adhesion and antifouling ability against liquids with complex components. Such superior self-cleaning properties highlight the significant value of this composite coating in practical engineering applications, including outdoor dust protection, antifouling, anti-particle deposition.

The fabrication of the SHS Cu is not limited to two-dimensional copper foil substrate. Using the same process parameters, superhydrophobic coatings can also be fabricated on 3D porous structures such as copper mesh and copper foam. The unmodified surfaces of copper mesh and copper foam exhibit smooth morphology (Figure S9a,b). Following alkaline etching and electrodeposition of CeO_2, both the copper mesh and copper foam surfaces developed a dense nanoneedle structure (Figure 7c). As a result, water droplets on these surfaces assumed a spherical shape with static WCAs exceeding 150°.

The corrosion behavior of SHS Cu was evaluated by potentiodynamic polarization measurements in 3.5 wt % NaCl solution. The corrosion potential (E_{corr}) and corrosion current density (I_{corr}) were determined by Tafel linear extrapolation. As shown in Figure 7d, bare Cu exhibited a corrosion current density (i^0_{corr}) of 3.148×10^{-5} A·cm^{-2}. In comparison, SHS Cu showed a positive shift in E_{corr}, while its corrosion current density (i_{corr}) decreased to 2.639×10^{-7} A·cm^{-2}. According to eq 2, the corrosion inhibition efficiency of SHS Cu was calculated to be 99.162% (Table 1). The reduced corrosion current density indicates that the SHS Cu surface effectively suppressed electrochemical corrosion in the chloride-containing medium.

The Nyquist plot shows that SHS Cu exhibits a significantly increased arc radius compared with pristine copper, implying an increase in charge transfer resistance (R_{ct}) (Figure 7e). The R_{ct} value characterizes the electron transfer process on the metal substrate surface. Generally, a larger R_{ct} corresponds to slower electron transfer and a lower corrosion rate. To quantitatively analyze the corrosion behavior of copper foil in saline solution, the electrochemical impedance spectroscopy (EIS) results were fitted using the equivalent circuit model (inset of Figure 7e). In this model, R_s represents the solution resistance, while CPE$_f$ and R_f correspond to the constant phase element (CPE) and resistance of the corrosion product film or coating on the copper surface, respectively. CPE$_{dl}$ is the CPE of the electric double layer, and R_{ct} signifies the charge transfer resistance. The fitting results reveal that the R_{ct} value of SHS Cu reached 4.013×10^4 Ω·cm^2, while that of bare copper was only 9.217×10^2 Ω·cm^2 (Table 2).

This demonstrates that the corrosion process on the superhydrophobic copper surface is remarkably suppressed. The Bode impedance plots further support this conclusion. The impedance modulus at the lowest frequency ($|Z|_{f=0.01Hz}$) is positively correlated with corrosion resistance. As illustrated in Figure S10a, the impedance modulus ($|Z|_{f=0.01Hz}$) for SHS Cu exceeds that of blank copper by more than an order of magnitude at 0.01 Hz. Moreover, SHS Cu maintained a high phase angle peak across a broad frequency range (Figure S10b), further confirming the enhanced corrosion resistance of the superhydrophobic coating. This high corrosion resistance and low corrosion tendency demonstrate that the superhydrophobic modification layer provides effective corrosion protection for the copper substrate, which is significant for prolonging the service life of copper materials in harsh environments such as marine settings.

4. CONCLUSIONS

This study presents a strategy for constructing superhydrophobic copper by integrating $Cu(OH)_2$ nanoneedle arrays with CeO_2 electrodeposition without intentionally added organic or fluorinated modifiers. The $Cu(OH)_2$ nanoneedle arrays provide the primary micro/nanoscale rough scaffold and a favorable interface for CeO_2 loading. DFT calculations indicate that CeO_2 adsorption is more favorable on $Cu(OH)_2$ than on bare Cu, further supporting the interfacial affinity between CeO_2 and $Cu(OH)_2$. CeO_2 deposition preserves the nanoneedle framework while increasing the arithmetic mean height from 1.355 to 2.297 μm. Subsequent vacuum heat treatment causes only a slight change to 2.328 μm without pronounced surface morphological reconstruction. Vacuum heating promotes surface dehydration and dehydroxylation, accompanied by the relative enrichment of nonpolar carbonaceous species, thereby reducing the affinity of the surface for water. The treated surface exhibits low-adhesion superhydrophobicity, with a water contact angle of 157.6° and a water-droplet adhesion force of 21.4 μN, together with mechanical durability, self-cleaning ability, repellency toward complex liquids, and stability in acidic, alkaline, and saline environments. Patterned superhydrophilic/superhydrophobic regions were also fabricated on a single copper substrate through selective masking and heat treatment. Electrochemical measurements demonstrated a corrosion inhibition efficiency of 99.162% in chloride-containing media. Moreover, this fabrication strategy features a simple procedure and can be readily extended to three-dimensional porous substrates such as copper mesh and copper foam, thereby offering new insights into the controllable fabrication and multifunctional applications of SHS Cu.

■ ASSOCIATED CONTENT

Supporting Information

The Supporting Information is available free of charge at https://pubs.acs.org/doi/10.1021/acsami.6c11391.

Experimental section and characterization including SEM, EDS, water contact angles, and dynamic water adhesion behavior measurements and bode modulus and bode phase angle plots of bare Cu and SHS Cu (DOCX)

Dynamic water adhesion behavior of the heat-treated $Cu(OH)_2$ nanoneedle surface with different CeO2 electro deposition time: 0min, 3min (Movie S1) (MP4)

Continuous bouncing process of water droplets on the SHS Cu (Movie S2) (MP4)

https://doi.org/10.1021/acsami.6c11391
ACS Appl. Mater. Interfaces 2026, 18, 48405−48416

Wettability difference of the patterned Cu surface before and after water immersion (Movie S3) (MP4)

Sliding behavior of various liquids (milk, coffee, juice, dying water, and mud slurry) on SHS Cu (Movie S4) (MP4)

AUTHOR INFORMATION

Corresponding Author

Jian Mao – *College of Material Science and Engineering, Sichuan University, Chengdu 610064, China;* orcid.org/0000-0001-7368-8537; Email: maojian@scu.edu.cn

Authors

Runxiang Tan – *College of Material Science and Engineering, Sichuan University, Chengdu 610064, China;* orcid.org/0000-0003-3907-7008

Kaiwen Yang – *College of Material Science and Engineering, Sichuan University, Chengdu 610064, China*

Complete contact information is available at: https://pubs.acs.org/doi/10.1021/acsami.6c11391

Author Contributions

All authors have given approval to the final version of the manuscript.

Funding

No funding was received for this work.

Notes

The authors declare no competing financial interest.

ACKNOWLEDGMENTS

Thank Professor Tao Gao from the Institute of Atomic and Molecular Physics, Sichuan University for providing the VASP software for DFT calculations.

REFERENCES

(1) Liu, H.; Ouyang, Y.; Li, B.; Zhou, Z.; Li, K.; Qiu, R. Bioinspired Superhydrophobic Coating on Copper: Electrochemical Fabrication, Characterization and Corrosion Inhibition. *J. Ind. Eng. Chem.* **2026**, *158*, 542−551.

(2) Ye, Y.; Kang, Z.; Wang, F.; Long, Y.; Guo, T.; Chen, D.; Kong, J.; Xu, L. Achieving Hierarchical Structure with Superhydrophobicity and Enhanced Anti-Corrosion via Electrochemical Etching and Chemical Vapor Deposition. *Appl. Surf. Sci.* **2023**, *610*, No. 155362.

(3) Feng, K.; Mei, H.; Chen, Y.; Yan, H.; Song, H.; Luo, C.; Guan, B.; Guan, H.; Monacelli, E.; Hu, Q.; Hu, Z. A Novel High Corrosion-Resistant and Superhydrophobic MAO-30/PA/VTES Composite Coating on Cu 15Fe Alloy for Long-Term Corrosion Protection. *Surf. Coat. Technol.* **2024**, *493*, No. 131287.

(4) Xiao, F.; Yuan, S.; Liang, B.; Li, G.; Pehkonen, S. O.; Zhang, T. Superhydrophobic CuO Nanoneedle-Covered Copper Surfaces for Anticorrosion. *J. Mater. Chem. A* **2015**, *3* (8), 4374−4388.

(5) Niu, S.; Fang, Y.; Qiu, R.; Qiu, Z.; Xiao, Y.; Wang, P.; Chen, M. Superhydrophobic Film Based on Cu-Dodecanethiol Complex: Preparation and Corrosion Inhibition for Cu. *Colloids Surf. Physicochem. Eng. Asp.* **2018**, *550*, 65−73.

(6) Shi, Z.; Ouyang, Y.; Qiu, R.; Hu, S.; Zhang, Y.; Chen, M.; Wang, P. Bioinspired Superhydrophobic and Oil-Infused Nanostructured Surface for Cu Corrosion Inhibition: A Comparison Study. *Prog. Org. Coat.* **2019**, *131*, 49−59.

(7) Benzarti, Z.; Arrousse, N.; Serra, R.; Cruz, S.; Bastos, A.; Tedim, J.; Salgueiro, R.; Cavaleiro, A.; Carvalho, S. Copper Corrosion Mechanisms, Influencing Factors, and Mitigation Strategies for Water Circuits of Heat Exchangers: Critical Review and Current Advances. *Corros. Rev.* **2025**, *43* (4), 429−455.

(8) Hatte, S.; Stoddard, R.; Pitchumani, R. Generalized Analysis of Dynamic Flow Fouling on Heat Transfer Surfaces. *Int. J. Heat Mass Transf.* **2022**, *188*, No. 122573.

(9) Li, B.; Li, X. One-Step Air Spraying of Structural Coating on Cu Alloy as Superhydrophobic Surface for Enhanced Corrosion Resistance and Anti-Icing Performance. *Materials* **2024**, *17* (18), No. 4485.

(10) Zhang, Y.; Li, B.; Zhang, S.; Zhao, H.; Wang, G.; Wu, P.; Liu, B.; Li, K. Corrosion-Resistant Superhydrophobic Composite Coating with Mechanochemical Durability. *Colloids Surf. Physicochem. Eng. Asp.* **2024**, *703*, No. 135186.

(11) Qiao, M.; Ji, G.; Lu, Y.; Zhang, B. Sustainable Corrosion-Resistant Superhydrophobic Composite Coating with Strengthened Robustness. *J. Ind. Eng. Chem.* **2023**, *121*, 215−227.

(12) Yang, T.; Zha, Z.; Wu, X.; Xiang, W.; Luo, Z.; Zhao, S. Superhydrophobic Coatings with Perfluorinated Metal−Organic Frameworks for Enhanced Corrosion Resistance. *Small* **2026**, *22* (14), No. e11751.

(13) Zhang, C.; Pei, K.; Sheng, T.; Zhang, M.; Zhao, Z.; Huang, W.; Li, Y.; Ai, S.; Guo, Z. Metal Oxides Engineering: Toward Sustainable Superhydrophobic Surfaces. *Adv. Funct. Mater.* **2026**, *36* (1), No. e12239.

(14) Tang, L.; Liu, X.; Zhang, X.; Yang, C.; Li, T.; Hu, C. Preparation of Copper-Manganese Superhydrophobic Coating with Self-Cleaning and Anticorrosion Resistance by One-Step Electrodeposition. *Colloids Surf. Physicochem. Eng. Asp.* **2024**, *692*, No. 134032.

(15) Zhang, Y.; Zhang, Z.; Yang, J.; Yue, Y.; Zhang, H. A Review of Recent Advances in Superhydrophobic Surfaces and Their Applications in Drag Reduction and Heat Transfer. *Nanomaterials* **2022**, *12* (1), No. 44.

(16) Liu, Y.; Bi, M.; You, Z.; Ma, R.; Fan, Y.; Du, A.; Zhao, X.; Yang, M. Fabrication of Corrosion-Resistant Superhydrophobic Nickel-cobalt Layered Double Hydroxide Coating on Copper Mesh for Oil-Water Separation. *J. Water Process Eng.* **2026**, *83*, 109607.

(17) Park, J.; Kim, D.; Kim, H.; Park, W. I.; Lee, J.; Chung, W. Superhydrophobic Electrodeposited Copper Surface for Robust Condensation Heat Transfer. *ACS Omega* **2022**, *7* (22), 19021−19029.

(18) Gaspar, G.; Salvador, M. A.; Pereira, M. J.; Carvalho, A. F.; Amaral, V. S.; Tedim, J.; Deuermeier, J.; Fernandes, A. J. S.; Silva, R. F.; Costa, F. M. Laser-Induced Copper Superhydrophobicity to Improve Heat Transfer and Reduce Limestone Deposition in Water Heating Systems. *Appl. Surf. Sci.* **2025**, *691*, No. 162614.

(19) Sun, Z.; Zhao, X.; Yuan, J.; Kong, G.; Lai, D.; Zheng, Y. Fabrication of Hybrid Micro-Nano Structure Superhydrophobic Surfaces by a Simple Nanosecond Laser Ablation and Chemical Modification Process. *Mater. Chem. Phys.* **2025**, *334*, No. 130480.

(20) Zhang, W.; Li, S.; Wei, D.; Zheng, Z.; Han, Z.; Liu, Y. Fluorine-Free, Robust and Self-Healing Superhydrophobic Surfaces with Anticorrosion and Antibacterial Performances. *J. Mater. Sci. Technol.* **2024**, *186*, 231−243.

(21) Hill, D.; Apsey, H.; Alexander, S. Recent Advances in Fluorine-Free Functionalized Nanomaterials for Low-Wettability Applications. *Curr. Opin. Colloid Interface Sci.* **2025**, *78*, No. 101922.

(22) Song, S.; Hu, Y.; Liu, Y.; Mao, J. Fabricating Stable and Self-Healing Superhydrophobic Photothermal-Responsive Coating without Modification towards Effective Anti-Corrosion and Anti-Icing. *Appl. Surf. Sci.* **2025**, *685*, No. 161980.

(23) Arnott, D. R.; Ryan, N. E.; Hinton, B. R. W.; Sexton, B. A.; Hughes, A. E. Auger and XPS Studies of Cerium Corrosion Inhibition on 7075 Aluminum Alloy. *Appl. Surf. Sci.* **1985**, *22* (23), 236−251.

(24) Fahrenholtz, W. G.; O'Keefe, M. J.; Zhou, H.; Grant, J. T. Characterization of Cerium-Based Conversion Coatings for Corrosion Protection of Aluminum Alloys. *Surf. Coat. Technol.* **2002**, *155* (2−3), 208−213.

(25) Hayes, S. A.; Yu, P.; O'Keefe, T. J.; O'Keefe, M. J.; Stoffer, J. O. The Phase Stability of Cerium Species in Aqueous Systems : I. E-pH Diagram for the System. *J. Electrochem. Soc.* **2002**, *149* (12), C623−C630.
(26) Edington, J.; O'Keefe, M. J.; O'Keefe, T. J. Development of a Spontaneous Immersion Process for Deposition of Cerium Oxide Coatings on Copper Substrates. *Surf. Coat. Technol.* **2006**, *200* (20−21), 5733−5737.
(27) Duan, Y.; Wang, X.; Gong, C.; Liu, J.; Cao, Y.; Li, H.; Gao, M. Vacuum-Induced Unmodified Superhydrophobicity on Co-CeO2-HEDP Surfaces for Synergistic Anti-Scaling, Self-Cleaning, and Reversible Wettability. *Colloids Surf. Physicochem. Eng. Asp.* **2025**, *727*, 138108.
(28) Azimi, G.; Dhiman, R.; Kwon, H.-M.; Paxson, A. T.; Varanasi, K. K. Hydrophobicity of Rare-Earth Oxide Ceramics. *Nat. Mater.* **2013**, *12* (4), 315−320.
(29) Oh, J.; Orejon, D.; Park, W.; Cha, H.; Sett, S.; Yokoyama, Y.; Thoreton, V.; Takata, Y.; Miljkovic, N. The Apparent Surface Free Energy of Rare Earth Oxides Is Governed by Hydrocarbon Adsorption. *iScience* **2022**, *25* (1), No. 103691.
(30) Preston, D. J.; Miljkovic, N.; Sack, J.; Enright, R.; Queeney, J.; Wang, E. N. Effect of Hydrocarbon Adsorption on the Wettability of Rare Earth Oxide Ceramics. *Appl. Phys. Lett.* **2014**, *105* (1), No. 011601.
(31) Nakayama, K.; Hiraga, T.; Zhu, C.; Tsuji, E.; Aoki, Y.; Habazaki, H. Facile Preparation of Self-Healing Superhydrophobic CeO_2 Surface by Electrochemical Processes. *Appl. Surf. Sci.* **2017**, *423*, 968−976.
(32) Liu, C.; Su, F.; Liang, J.; Huang, P. Facile Fabrication of Superhydrophobic Cerium Coating with Micro-Nano Flower-like Structure and Excellent Corrosion Resistance. *Surf. Coat. Technol.* **2014**, *258*, 580−586.
(33) Ren, A.; Fu, X.; Duan, S.; Shen, M.; Lin, J. Effect of Current Density on the Performance of Ni-Fe-P-CeO_2 Composite Coating Prepared by Jet Electrodeposition. *Int. J. Electrochem. Sci.* **2020**, *15* (9), 8563−8583.
(34) Xue, Y.; Wang, S.; Xue, Y.; Cao, L.; Nie, M.; Jin, Y. Robust Self-Cleaning and Marine Anticorrosion Super-Hydrophobic Co−Ni/CeO_2 Composite Coatings. *Adv. Eng. Mater.* **2020**, *22* (11), No. 2000402.
(35) Fathyunes, L.; Mohtadi-Bonab, M. A. Co-Electrodeposition of Superhydrophobic NiCo/CeO_2 Coating with Hierarchical Nano/Micro Structure for Corrosion Protection of Plain Carbon Steel. *Mater. Today Commun.* **2024**, *39*, No. 108851.
(36) Perdew, J. P.; Burke, K.; Ernzerhof, M. Generalized Gradient Approximation Made Simple. *Phys. Rev. Lett.* **1996**, *77* (18), 3865−3868.
(37) Verlato, E.; Comisso, N.; Mattarozzi, L.; Musiani, M.; Vázquez-Gómez, L. New Evidence on the Electroprecipitation of Ceria. *Electrochim. Acta* **2024**, *492*, No. 144344.
(38) Luo, Y.; Li, J.; Zhu, J.; Zhao, Y.; Gao, X. Fabrication of Condensate Microdrop Self-Propelling Porous Films of Cerium Oxide Nanoparticles on Copper Surfaces. *Angew. Chem., Int. Ed.* **2015**, *54* (16), 4876−4879.
(39) Wenzel, R. N. Resistance of Solid Surfaces to Wetting by Water. *Ind. Eng. Chem.* **1936**, *28* (8), 988−994.
(40) Chen, F.; Wang, Y.; Tian, Y.; Zhang, D.; Song, J.; Crick, C. R.; Carmalt, C. J.; Parkin, I. P.; Lu, Y. Robust and Durable Liquid-Repellent Surfaces. *Chem. Soc. Rev.* **2022**, *51* (20), 8476−8583.
(41) Cassie, A. B. D.; Baxter, S. Wettability of Porous Surfaces. *Trans. Faraday Soc.* **1944**, *40*, No. 546.
(42) Cormican, C. M.; Bektaş, S.; Martin-Martinez, F. J.; Alexander, S. Emerging Trends in Bioinspired Superhydrophobic and Superoleophobic Sustainable Surfaces. *Adv. Mater.* **2025**, *37* (12), No. 2415961.
(43) Zhang, B.; Dai, Z.; Chen, Y.; Cheng, M.; Zhang, H.; Feng, P.; Ke, B.; Zhang, Y.; Zhang, G. Defect-Induced Triple Synergistic Modulation in Copper for Superior Electrochemical Ammonia Production across Broad Nitrate Concentrations. *Nat. Commun.* **2024**, *15* (1), No. 2816.
(44) Zhang, G.; Liu, X.; Wang, L.; Xing, G.; Tian, C.; Fu, H. Copper Collector Generated Cu^+ /Cu^{2+} Redox Pair for Enhanced Efficiency and Lifetime of Zn−Ni/Air Hybrid Battery. *ACS Nano* **2022**, *16* (10), 17139−17148.
(45) Zhang, W.; Wen, X.; Yang, S. Controlled Reactions on a Copper Surface: Synthesis and Characterization of Nanostructured Copper Compound Films. *Inorg. Chem.* **2003**, *42* (16), 5005−5014.
(46) He, D.; Wang, G.; Liu, G.; Bai, J.; Suo, H.; Zhao, C. Facile Route to Achieve Mesoporous $Cu(OH)_2$ Nanorods on Copper Foam for High-Performance Supercapacitor Electrode. *J. Alloys Compd.* **2017**, *699*, 706−712.
(47) Ji, Y.; Jin, Z.; Li, J.; Zhang, Y.; Liu, H.; Shi, L.; Zhong, Z.; Su, F. Rambutan-like Hierarchically Heterostructured CeO_2-CuO Hollow Microspheres: Facile Hydrothermal Synthesis and Applications. *Nano Res.* **2017**, *10* (2), 381−396.
(48) Li, X.-P.; Sun, Y.-L.; Xu, Y.-Y.; Chao, Z.-S. UV-Resistant and Thermally Stable Superhydrophobic CeO_2 Nanotubes with High Water Adhesion. *Small* **2018**, *14* (27), No. 1801040.
(49) Yan, X.; Huang, Z.; Sett, S.; Oh, J.; Cha, H.; Li, L.; Feng, L.; Wu, Y.; Zhao, C.; Orejon, D.; Chen, F.; Miljkovic, N. Atmosphere-Mediated Superhydrophobicity of Rationally Designed Micro/Nanostructured Surfaces. *ACS Nano* **2019**, *13* (4), 4160−4173.

https://doi.org/10.1021/acsami.6c11391
ACS Appl. Mater. Interfaces 2026, 18, 48405−48416